Probabilistic Spatio-temporal Seasonal Sea Ice Presence Forecasting using Sequence to Sequence Learning

Nazanin Asadi[1], Philippe Lamontagne[2], Matthew King[2,3], Martin Richard[2], and K Andrea Scott[1]

[1]Department of Systems Design Engineering, University of Waterloo, Waterloo, Canada
[2]Ocean, Coastal and River Engineering Research Centre, National Research Council Canada, Ottawa, Canada
[3]Memorial University of Newfoundland, Newfoundland and Labrador, Canada.

Correspondence: Nazanin Asadi (n2asadi@uwaterloo.ca)

Abstract. Accurate and timely forecasts of sea ice conditions are crucial for safe shipping operations in the Canadian Arctic and other ice-infested waters. Given the recent declining trend of Arctic sea ice extent in past decades, seasonal forecasts are often desired. In this study machine learning (ML) approaches are deployed to provide accurate seasonal forecasts based on ERA5 data as input. This study, unlike previous ML approaches in the sea-ice forecasting domain, provides daily spatial maps of sea ice presence probability in the study domain for lead times up to 90 days using a novel spatio-temporal forecasting method based on sequence-to-sequence learning. The predictions are further used to predict freeze-up/break-up dates and show their capability to capture these events within a seven day period at specific locations of interest to shipping operators and communities. The model is demonstrated in hindcasting mode to allow evaluation of forecasted predication. However, the design allows the approach to be used as a forecasting tool.

1 Introduction

Spatial and temporal forecasts of sea ice concentration (fraction of a given area covered by sea ice) are carried out at various scales to address the requirements of different stakeholders (Guemas et al., 2016). Short-term forecasts (1-7 days) at high spatial resolution (5-10 km) are important for day-to-day operations and weather forecasting (Carrieres et al., 2017; Dupont et al., 2015), whereas longer term (60-90 day) forecasts are desired by shipping companies and offshore operators in the Arctic for strategic planning (Melia et al., 2016). In this study we are interested in these longer term forecasting methods, which we will refer to as seasonal forecasting. Typical approaches are usually statistical or dynamical in nature. Statistical models have included multiple linear regression (Drobot et al., 2006), or Bayesian linear regression (Horvath et al., 2020), whereas by dynamical approaches we are referring to those that use a forecast model solving the prognostic equations governing evolution of the ice cover (Askenov et al., 2017; Sigmond et al., 2016). An excellent overview of both statistical and dynamical approaches is given in (Guemas et al., 2016).

An early study on seasonal sea ice forecasting using a dynamical approach is that by Zhang et al. (2008) in which they evaluated the ability of an ensemble of sea ice states from a coupled ice-ocean model to predict the spring and summer Arctic sea ice extent and thickness for the year of 2008, following the anomalously warm year of 2007. Each ensemble member was generated by forcing the coupled ice-ocean model with atmospheric states from one of the previous seven years, and

25 running the model forward in time for one year. A comparison between pan-Arctic and regional forecast skill was carried out by Bushuk et al. (2017), where skill was assessed using the detrended anomaly correlation coefficient (ACC) of sea ice extent. It was shown that the ACC of seasonal forecasts in specific regions was dependent on the region and forecast month.

Dynamical forecast models solve differential equations describing the physics of the underlying system. Solution methods for these types of equations are well-known and relatively robust. A key challenge with these models in operational forecasting
30 is the high level of computational resources required to generate a forecast. This disadvantage can be overcome by using statistical approaches such as multi-linear regression (Drobot et al., 2006) or canonical correlation analysis (Tivy et al., 2011). Both of these approaches determine a linear relationship between a set of predictor variables and a set of predictands.

More recently, convolutional neural networks (CNNs), which are able to learn nonlinear relationships between spatial patterns in input data and predictands, have been used for sea ice concentration prediction (Kim et al., 2020). The study by Kim
35 et al. (2020) used eight predictors composed of sea ice concentration data and variables from reanalyses to train 12 individual monthly models, and produced monthly spatial maps of sea ice concentration (SIC). Their method was able to predict mean September sea ice extent in good agreement with that from from passive microwave data, evaluated for the year of 2017, where the sea ice extent is the total area in a given region that has at least 15% of ice cover. Similar to Kim et al. (2020), Horvath et al. (2020) focused on the September sea ice extent. Hovath et al. (2020) used a Bayesian logistic model to predict both a monthly
40 average sea ice concentration and an uncertainty. The model inputs were atmospheric and oceanic predictor variables and sea ice concentration from satellite data. It was found that the uncertainty was higher at the ice edge, although further analysis of this output was not given. Another recent study, (Fritzner et al., 2020) compared two machine learning (ML) approaches, K-nearest-neighbour (KNN) and fully convolutional neural networks, with ensemble data assimilation.

A recent approach close to the one presented here is IceNet (Andersson et al., 2021), which trained an ensemble of CNNs
45 to produce monthly maps of sea ice presence (probability SIC > 15%) for forecast lengths up to 6 months. Similar to other studies, input to this model consisted mainly of reanalysis data. A novel aspect was the training protocol, which consisted of pre-training each ensemble member using a long time series of data from the Coupled Model Intercomparison Project phase 6 (CMIP6) and then fine-tuning the trained CNNs using sea ice concentration observations, followed by a scaling method, known in the ML community as 'temperature scaling', to produce a calibrated probability of sea ice presence.

50 None of the previously proposed ML approaches produce a forecast that propagates in space and time, or a *spatiotemporal* forecast. In this study we investigate a sequence-to-sequence (Seq2Seq) learning approach to provide daily spatiotemporal forecasts of the probability of sea ice presence (probability SIC > 15%) over the region of Hudson Bay, with forecast lead times up to 90 days. To keep the method general, we use ERA5 data as input to our model. By using the Seq2Seq approach we are able to produce forecasts over a different number of days than our training sequence. The method is similar to operational
55 forecasting studies (Chevallier et al., 2013; Sigmond et al., 2013), where an initial state is propagated forward in time, except we are using a data-driven machine learning approach, as compared to a physics-based model, and our forecasted variable is a number between 0 and 1 that indicates an (uncalibrated) probability of sea ice presence at a grid location, as compared to sea ice concentration.

2 Data

The present study utilizes ERA5 reanalysis data for model predictors and validation. ERA5 is a recent reanalysis produced by the European Center for Medium Range Weather Forecasting (ECMWF). It consists of an atmospheric reanalysis of the global climate providing estimates of a large number of atmospheric, land and oceanic climate variables. The spatial resolution is $\approx$31 km and reanalysis fields are available every hour from 1979 - present (Wang et al., 2019). Observations are assimilated into the atmospheric model using a 4D-Variational data assimilation scheme. In this study ERA5 reanalysis data from 1985-2017 are used.

The sea ice concentration data used in ERA5 is from the EUMETSAT Ocean and Sea Ice Satellite Applications Facility (OSI-SAF) 401 dataset (Tonboe et al., 2016). These data are produced using a combination of passive microwave sea ice concentration retrieval algorithms to benefit from low sensitivity to atmospheric contamination of the surface signal, while maintaining an ability to adapt to changes in surface conditions through the use of variable tie-points for ice and water (Tonboe et al., 2016). Although the SIC is gridded to a 10 km grid, the spatial resolution of these data is limited by the instrument field of view of the 19 GHz channel used in the SIC retrieval, which is 45 km $\times$ 69 km. When the SIC data are ingested into ERA5 the SIC values that are less that 15% are set to zero. Additionally, SIC is set to zero if sea surface temperature (SST) is above a specified threshold to account for known biases in passive microwave sea ice concentration during melt.

The current study utilizes daily samples with the following eight input variables from ERA5 dataset over the period of 1985-2017: sea ice concentration, sea surface temperature, 2m temperature (t2m), surface sensible heat flux, wind 10 meter U-component (u10), wind 10 meter V-component (v10), landmask and additive degree days (ADD) derived from the t2m variable. All the input variables except sea ice concentration and landmask are normalized before being input to the network. Recalling that data are available from ERA5 every hour, the fields from 12:00 (midday) were used.

There were some irregularities with the ERA5 landmask file and the sea ice concentration. Some locations indicated as land in the landmask file had a non-zero sea ice concentration value. At these locations the sea ice concentration was set to zero. There were also some locations indicated as non-land in the landmask file that had a zero ice concentration, even when the ice concentration should be non-zero based on the atmospheric conditions, season, and examination of the time-series at the given location. At these locations the sea ice concentration was set to the average of the non-land neighboring pixels.

3 Study Region

For the present study we focus on the Hudson Bay System, consisting of Hudson Bay, James Bay, Hudson Strait and Foxe Basin (Fig. 1). The area is bordered by 39 communities, where 29 of them are exclusively accessible by sea or air. These communities rely extensively on sealift operations during the ice-free season to receive their yearly resupply of fuel and goods too heavy to be flown. Shipping traffic, mostly confined during the ice-free and shoulder seasons, is also generated by mining, fishing, tourism and research activities (Andrews et al., 2018). The study area is seasonally covered by first-year ice, with open water over most of the domain each summer, with the exception of some small regions in Foxe Basin. The seasonal cycle of ice cover in this region is dominated by local atmospheric and oceanic drivers (Hochheim and Barber, 2014). Freeze-up generally
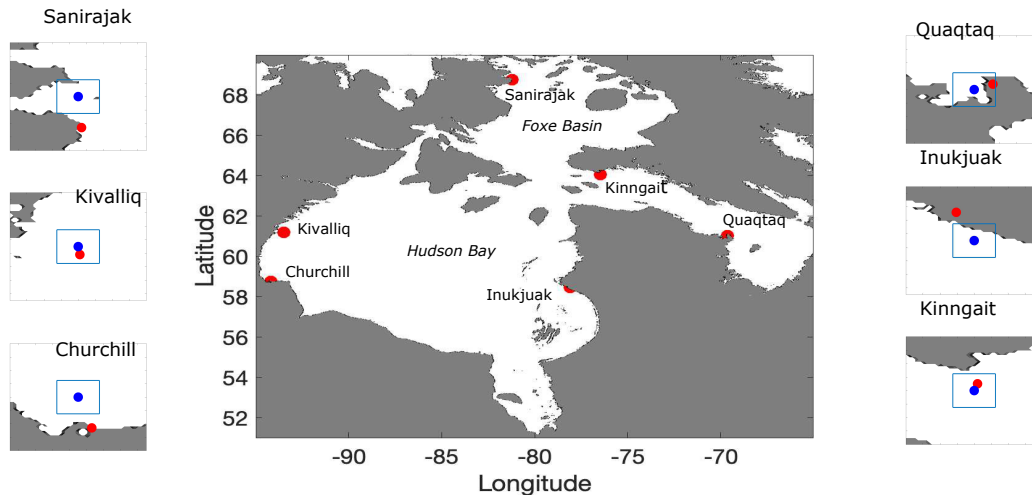
Figure 1. The study region with locations of interest shown in red. The insets show the location of a nearby port or polynya (red) and the nearest point on the model grid (blue) that is outside of the land boundary (where landmask from ERA5 is less than 0.6), in addition to a bounding box that approximates a grid cell. The model grid point near Quaqtaq is located (correctly) in the water region because the landmask from ERA5 has a low value in that region due to the low elevation. The ports are Churchill, Inukjuak and Quaqtaq, whereas the polynyas are near Sanirajak, Kivalliq and Kinngait.

starts in November (earlier in the northern part of the region) and lasts for a couple of months. Break-up usually starts in May or June, and the break-up period is a little longer than freeze-up, at 2-3 months. Recent years show earlier break-up and later freeze-up. The trends and their significance are dependent on the region (Hochheim and Barber, 2014; Andrews et al., 2018).

4   Forecast model architecture

The seasonal forecasting problem of this study can be formulated as a spatiotemporal sequence forecasting problem that can be solved under the general sequence-to-sequence (Seq2Seq) learning framework (Sutskever et al., 2014). In Seq2Seq learning, which has successful applications in machine translation (Cho et al., 2014), video captioning (Venugopalan et al., 2015), speech recognition (Chiu et al., 2018), the target is to map a sequence of inputs to a sequence of outputs, where the inputs and outputs can be different lengths. The architecture of these models normally consists of two major components; encoder and decoder. The encoder component transforms a given input (here, a set of geophysical variables such as sea ice concentration, air temperature etc.) to an encoded state of fixed shape, while the decoder takes that encoded state and generates an output sequence (here, a sea ice presence probability) with the desired length, which here is the number days in the forecast (90 days).

For this study, following the encoder-decoder architecture described above, two spatial-temporal sequence-to-sequence prediction models are developed. These will be referred to herein as the "Basic Model" and "Augmented Model" and are described in Sections 4.1 and 4.2 respectively. For both models, the prediction sequence is unrolled over a user-specified number of fore-

cast days to produce ice presence probability forecasts on a spatial grid each day with a scale of ≈ 31 km (the same as the ERA5 input data).

4.1 Basic model

110 The encoder section of the Basic model takes the geophysical variables from the last three days (sea ice concentration, air temperature etc.) as input. Each input sample is of size $(3 \times W \times H \times C)$ where 3 is the number of historical days, W and H are the width and height of the raster samples in their original resolution and C is the total number of input variables (here eight). Using a longer input sample of 5 days was also tested, but did not lead to an improvement in forecast quality. With this longer input the quantity of data to be processed was greater than that for 3 days, which increased the computational expense 115 and data storage requirements, hence 3 days were used for the experiments shown here.

The overall architecture is shown in Fig 2a. The encoder starts by passing each input sample through a feature pyramid network (Lin et al., 2017) to detect spatial patterns in the input data at both the local and large scales. Next, the sequence of feature grids extracted from the feature pyramid network are further processed through a convolutional LSTM (long short-term memory) layer (ConvLSTM) (Hochreiter and Schmidhuber, 1997; Xingjian et al., 2015), returning the last output state. This 120 layer learns a single representation of the time series that also preserves spatial locality. The most recent day of historic input data is concatenated with the ConvLSTM output to better preserve the influence of this state on the model predictions. The encoder provides as output a single raster with the same height and width as the stack of raster data input to the network, but with a higher number of channels such as fully represent the encoded state. The final encoded state is then fed to a custom recurrent neural network (RNN) decoder that extrapolates the state across the specified number of time-steps. It takes as input 125 the encoded state with multiple channels and as output produces a state with the same height and width as the input over the desired number of time-steps in the forecast (here 90 days). Finally, a time-distributed network-in-network (Lin et al., 2013) structure is employed to apply a 1D convolution on each time-step prediction to keep the spatial grid size the same but reduce the number of channels to one, representing the daily probabilities of sea ice presence over the forecast period (up to 90 days).

The custom RNN decoder, shown in Fig 2b, as is common of many RNN layers, maintains both a cell state and a hidden state 130 (Yu et al., 2019). First, the initial cell state and hidden state are initialized with the input encoded state. Then, at each time-step and for each of the states, the network predicts the difference, or residual, from the previous state to generate the updated states using depthwise separable convolutions (Howard et al., 2017). The output of the decoder section is the concatenation of the cell states from each time-step.

4.2 Augmented model

135 A slight variant of the Basic model, referred to as the Augmented model, is developed to accept a second input. This second input has the same height and width as the first input but corresponds to Climate Normal of three variables over the required period (e.g. 90 days), where these variables are t2m, u10 and v10 and their Climate Normal is calculated from 1985 to the last training year for each forecast day. These variables were chosen because of their availability in both historical data sets, and real time (for this application, through the Meteorological Service of Canada GeoMet platform). Since this branch of the network

a) Overall architecture
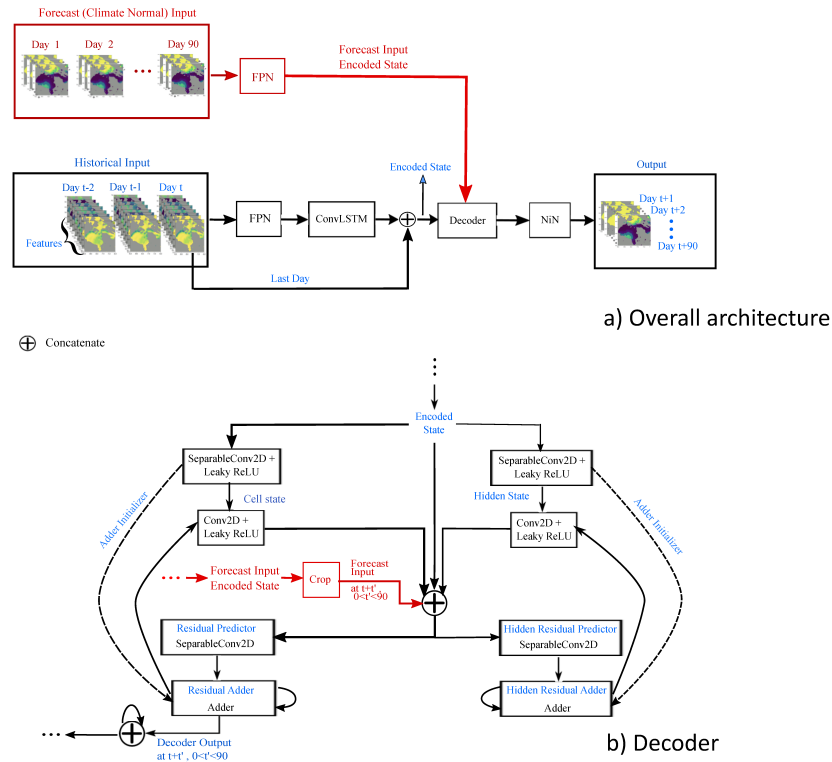
b) Decoder

Figure 2. Overall network architecture(a) and custom decoder (b). The red portion refers to the additional components required for the augmented model. The dashed arrows show a process carried out only once (the initialization of the adder). FPN refers to the feature pyramid network, ConvLSTM, the convolutional long short-term memory network, NiN is the network in network module.

'augments' the core model, it was desired to keep this flexibility for future development as our computing infrastructure is designed to connect with GeoMet. For the augmented model, the original encoder structure for historical input data remains unchanged, but a secondary encoder is added to the network, consisting of a feature pyramid network, that receives the Climate Normal data as input. A secondary variant of the decoder component is implemented, which accepts this encoded forecast sequence in order to enhance estimates of the residuals at each of the future time-steps (see Fig 2).

5 Description of Experiments

Since the overarching goal is to provide a tool to stakeholders that can be used operationally, a training and validation protocol is required that truly assesses the forecasting skills without using future data. For example, on this basis a leave-one-out approach cannot be used. Instead, we initially train over a given number of years, then we update the model weights (retrain, initializing with current weights) for future training periods. We tested different initial training periods (10 years vs 20 years) and also different numbers of months to include in training our monthly models. The current protocol (Fig 3) led to the best results. In
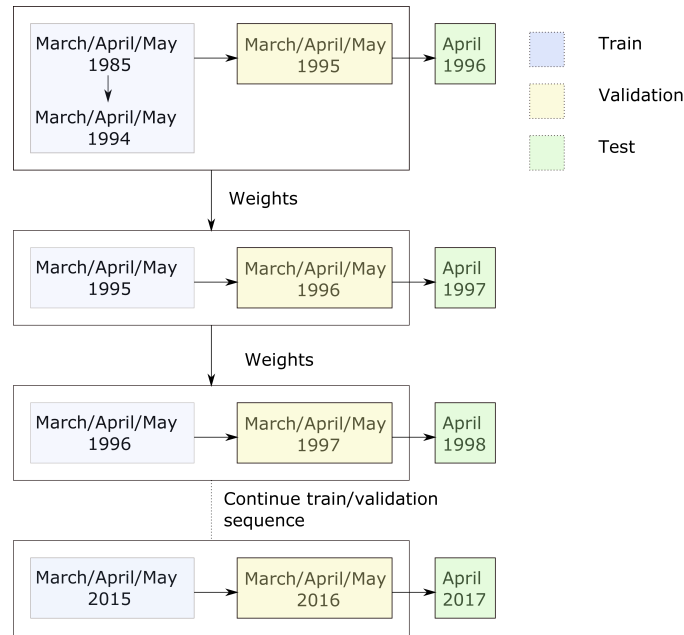
Figure 3. Training, validation and test protocol used for both the Basic and Augmented model.

this protocol for each month of a year a separate model is trained on data from the given month as well as the preceding and following month. For example, the 'April model' is trained using data from March 1 to May 31. This monthly model is initially trained on data from a fixed number of years, chosen to be 10 years, as a compromise between having enough data to provide the model with representative conditions from which it can learn, while allowing enough data to be set aside for validation and testing. After this initial experiment, to predict each following test year i, using a rolling forecast prediction, the weights of the model from year $i-1$ are updated with data from year $i-2$. Data for year $i-1$ is used as validation for early stopping criteria and to evaluate the training performance. For example, if the initial model is trained on 10 years, data from year 11 is used as validation and first predictions are launched at year 12. The model for year 11 is initialized with weights from the 10-year model, which are updated with data from year 10, validated on year 11 and used to predict year 12. The model for year 12 is then initialized with weights from the year 11 model, which are updated with data from year 11, validated on year 12, and used to predict year 13. This process is used to produce forecasts of sea ice presence for years 1996 to 2017. Since the weight updates only uses data of one year for training and validation, it is computationally fast and efficient.

The ML models are implemented using the TensorFlow Keras open-source library with stochastic gradient descent (SD) optimizer with learning rate of 0.01, momentum of 0.9 and binary cross-entropy loss function. The maximum training epoch for the initial model and the retraining process is 60 and 40 respectively and for both cases the training process stops if the validation accuracy is not improved after 5 epochs.

6 Skill Scores

In order to evaluate the performance of the ML models, two different skill scores are used. The first is the binary accuracy, and the second is the Brier score. Binary accuracy is calculated by mapping the ML model forecasts, which denote a probability of sea ice presence, to binary values by thresholding the probability such that when $P > 0.5$ the pixel is considered to be ice and when $P \leq 0.5$ it is considered to be water (similar to Andersson et al. (2021)). After this thresholding, the binary accuracy is calculated as $(TP + TN)/N$, where TP denotes a true positive, and has a value of one if both the pixel in the model and observations are one (indicating ice), and a value of zero otherwise; TN denotes a true negative, and has a value of one if both the pixel in the model and observations are zero (indicating water); and N is the total number of points considered. Binary accuracy is used to calculate monthly scores, in which case N is the product of the number of points in the spatial domain, the days in the given month and the number of years over which the forecasts are evaluated. For binary accuracy a score of one is considered optimal.

Binary accuracy scores do not differentiate between a predicted probability of 0.51 and 0.9. Both would be a true positive if the pixel is ice in the observations. For binary accuracy, small changes in the predicted probability around the probability threshold impact the binary accuracy. An alternative score that better reflects the value of the predicted probability is the Brier score (BS) (Ferro, 2007),

$$BS = \frac{1}{M}\frac{1}{T}\sum_{i=1}^{M}\sum_{t=1}^{T}(P_{t,i} - O_{t,i})^2, \tag{1}$$

where $P_{t,i}$ is the model prediction (sea ice presence probability) and $O_{t,i}$ is the corresponding observation (zero or one), at time t, and grid location i; M represents the total number of points in the spatial domain and T the total number of temporal outputs used (note $N = M * T$). For the Brier score a value of zero is considered optimal.

To provide a baseline, we also compare our ML models to a Climate Normal, which is defined here as the average of the sea ice presence from 1985 to the last year in the training set for each experiment. While inputs of each model in training and test procedure are derived from three months of each year, only the results from the central month (2nd of three) are selected to evaluate the results of the given model. For example, the April model is trained using historical data from March-April-May. This model is evaluated by extracting the 90-day forecasts launched during the month of April. The observations are sea ice presence from ERA5 (test data in Fig 3).

7 Results

7.1 Forecasts of Ice Presence

7.1.1 Monthly averaged results

For each day in the test set, which is the set of days over which the 90 day predictions are launched, we have 90 binary accuracy maps of our study region. The monthly statistics are summarized in Fig 4(a,b,c). For example, each value at index (i, j) of panel

(a) Climate Normal   (b) Basic model   (c) Augmented model

(d) Basic model-Climate Normal   (e) Augmented model-Climate Normal   (f) Augmented model-Basic model
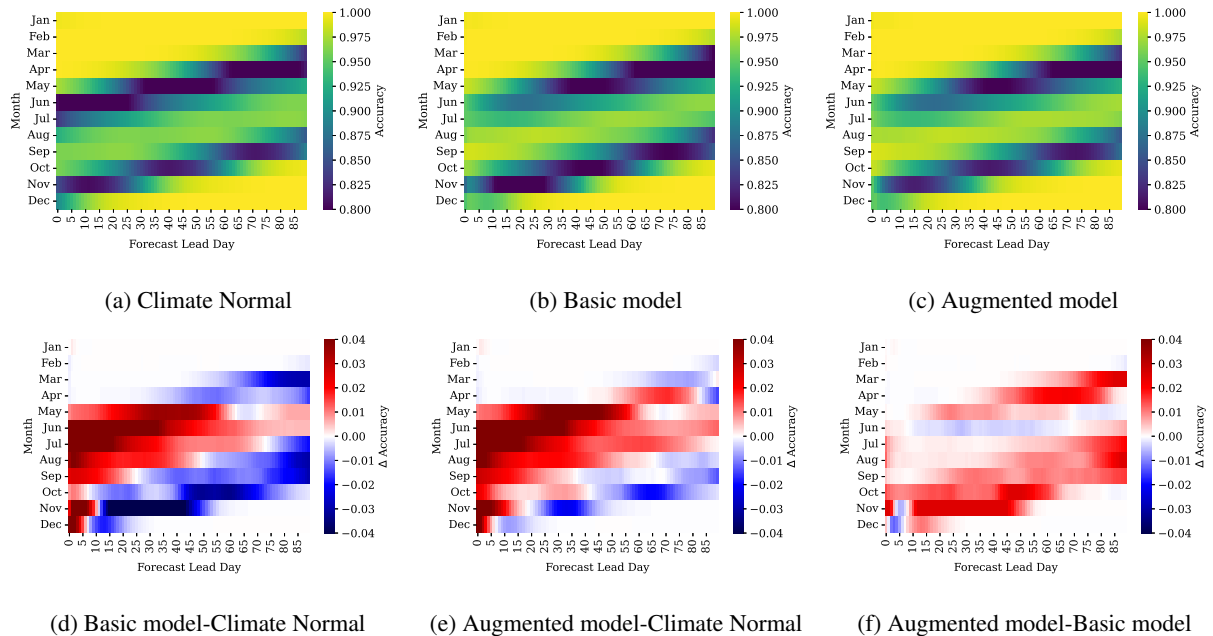
Figure 4. Binary accuracies as a function of lead time. Top row panels show the binary accuracy of each model (a)-(c) while bottom row panels show the differences in binary accuracy between the models (d-f). The Augmented model is trained with additional 90-day Climate Normal input. Most differences are observed in the break-up and freeze-up seasons.

(a) and (b) of Fig 5 represents the average binary accuracy score of all predictions in the test set that are launched at month i at lead day j where $1 \leq i \leq 12$ and $1 \leq j \leq 90$. The $(1,1)$ index value of Fig 4a shows the binary accuracy of 1-day forecasts launched between January 1 and 31, ending January 2 to February 1. The $(1,2)$ index value corresponds to the binary accuracy of 2-day forecasts. These forecasts were launched between January 1 to 31 ending January 3 to February 2. This continues until the 90-day forecast box is reached (top-right box in Panel 1b), corresponding to forecasts ending April 1-30.

The binary accuracies are close to 100% for the month of January and for lead times that cover the months of January, February and March, as would be expected, because at this time the region is covered with ice (Fig 2 a,b,c). In contrast, for forecasts at the beginning of the open water season (June and July), Climate Normal struggles to accurately capture the ice cover for lead times of 1 to 50 days (Fig 4a), likely due to inter-annual variability and lengthening of the open water period (Hochheim and Barber, 2014; Andrews et al., 2018). The Basic and Augmented models have higher accuracies than Climate Normal over these months (Fig 4d). We also note improvements in the Basic and Augmented models at early lead times for August, September, October and November, as compared to Climate Normal (Fig 4d,e). Improvements can be seen in particular for longer lead times in July/August, and at shorter lead times (15-50 days) for November. These forecasts correspond to the freeze-up period, which starts in mid-October or November in the study region and lasts for approximately two months (Hochheim and Barber, 2014).

(a) Basic model   (b) Augmented model   (c) Augmented model-Basic model
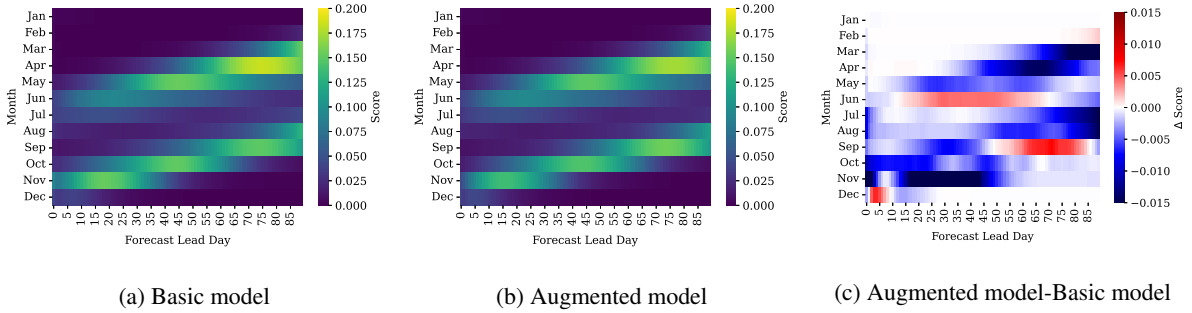
Figure 5. Brier score of the Basic (a) and Augmented (b) model as a function of lead time. Their score difference is shown in (c). Most differences are observed in the break-up and freeze-up seasons.

Figure 5 presents the monthly averaged Brier scores for the Basic and Augmented models (Fig 5a and b), and their differences (Fig 5c) as a function of lead day. Similar to Fig 4, each value at index (i, j) of panel (a) and (b) of Fig 5 represents the average Brier score of all predictions in the test set that are launched at month i at lead day j where $1 \leq i \leq 12$ and $1 \leq j \leq 90$. The resulting pattern is similar to that for binary accuracy. Recalling that a Brier score of zero is optimal, the higher Brier scores seen during freeze-up and break-up for both models indicates poorer performance during these seasons. Their difference (Fig. 5c) indicates a better score for the Augmented model at longer lead times especially for March, April, July and August. In contrast for some cases like 60-90 lead day forecasts of the September model the Brier score of the Basic model is around 0.01 better than the Augmented model. The reason for the higher Brier score of the Basic model in comparison to the Augmented model here may be because the September model uses training data over August-October. The trend over this period may be less representative of more recent ice conditions (Hochheim and Barber, 2014; Andrews et al., 2018), which may make the additional data used in the Augmented model un-helpful at these longer forecast periods.

The calibration curves of the Basic and Augmented September models are shown in Figure 6. These curves represent the observed frequency of ice presence, where the frequency is calculated over the entire domain, versus the forecasted probabilities for different lead days of forecasts launched in September. For early lead days both models, especially the Basic model, show close to perfect calibration (blue line) but at 60 lead day the underestimation is more significant for the Augmented model with lower forecasted probabilities of ice in comparison to observations, while at 90 lead day the overestimation is more significant for the Augmented model, with a forecasted probability that is much higher than the observed frequency of ice. This suggests that in comparison to observations, freeze-up may be delayed at 60 lead days for regions with freeze-up dates around November and may be too early at 90 lead days for regions with freeze-up date around December for the Augmented model.

7.1.2 Spatial maps of sea ice presence

Binary accuracy values averaged over the domain and each month do not provide information about model performance at each location in the spatial domain, or at a finer time scale. The model proposed here provides a spatial map of the probability of ice for each day in the forecast period. In Fig 7 the spatial distribution of ice and water is shown with the probability of ice

| (a) Basic model | (b) Augmented model |
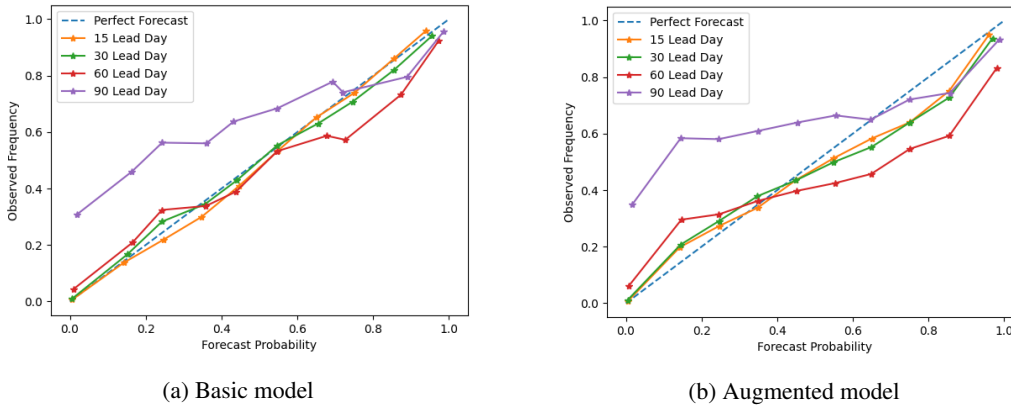
Figure 6. Calibration curves for the Basic and Augmented model for sea ice presence forecasts initiated from September 1st to 30th for different lead days. At 90 lead days, both models underestimate the probability of sea ice when observed frequencies are less than 0.75 and overestimate the probability of sea ice at higher probabilities. The Basic model is well-calibrated for short lead times.

for three different dates during the break-up period. The observations are ice and water obtained by applying a threshold of 15% to SIC from ERA5 for the given date. For example, given that the forecasts are launched on May 6th 2014, the left column (after 30 days) corresponds to the sea ice state on June 5th 2014.

The forecast after 30 days indicates both the Basic and Augmented models predict a reduced ice presence probability along the east coast of Hudson Bay that is in better agreement with observations than Climate Normal. Similarly, after 50 and 70 days, Climate Normal has a higher ice cover relative to the lower probability of ice for the Basic Model in the central part of Hudson Bay, while the Augmented model is in better agreement with observations. In comparing the probability maps for the Basic and Augmented model, it can be noted the Basic model has reduced ice presence probability in the southern part of the domain and increased ice presence probability in the northern part of the domain. Overall we find the spatial pattern of break-up to be in good agreement with the observations, in particular for the Augmented model.

7.2 Assessment of Operational Freeze-up and Break-up date forecasting

7.2.1 Freeze-up and Break-up Accuracy

The accuracy of the model in predicting freeze-up and break-up date is indicative of operational capability of the trained models to support shipping operations during the shoulder season. Following the definition used by the Canadian Ice Service (CIS), the freeze-up date of each pixel in a year is the first date in the freeze-up season (October 1st to January 31st for Hudson Bay) that ice (value of 1 after thresholding the predicted probabilities at 50%) is observed for 15 continuous days. A similar procedure is carried out to predict break-up, with the exception that the pixel must be considered water (value of 0 after thresholding its predicted probability) for 15 continuous days for break-up to have occurred in the break-up season (May 1st to July 31st for Hudson Bay, with forecasts initialized up to July 31st considered). These per pixel per year freeze-up/break-up dates are calculated for observations, Climate Normal and model predictions at 30 and 60 lead days. To obtain each accuracy map, first
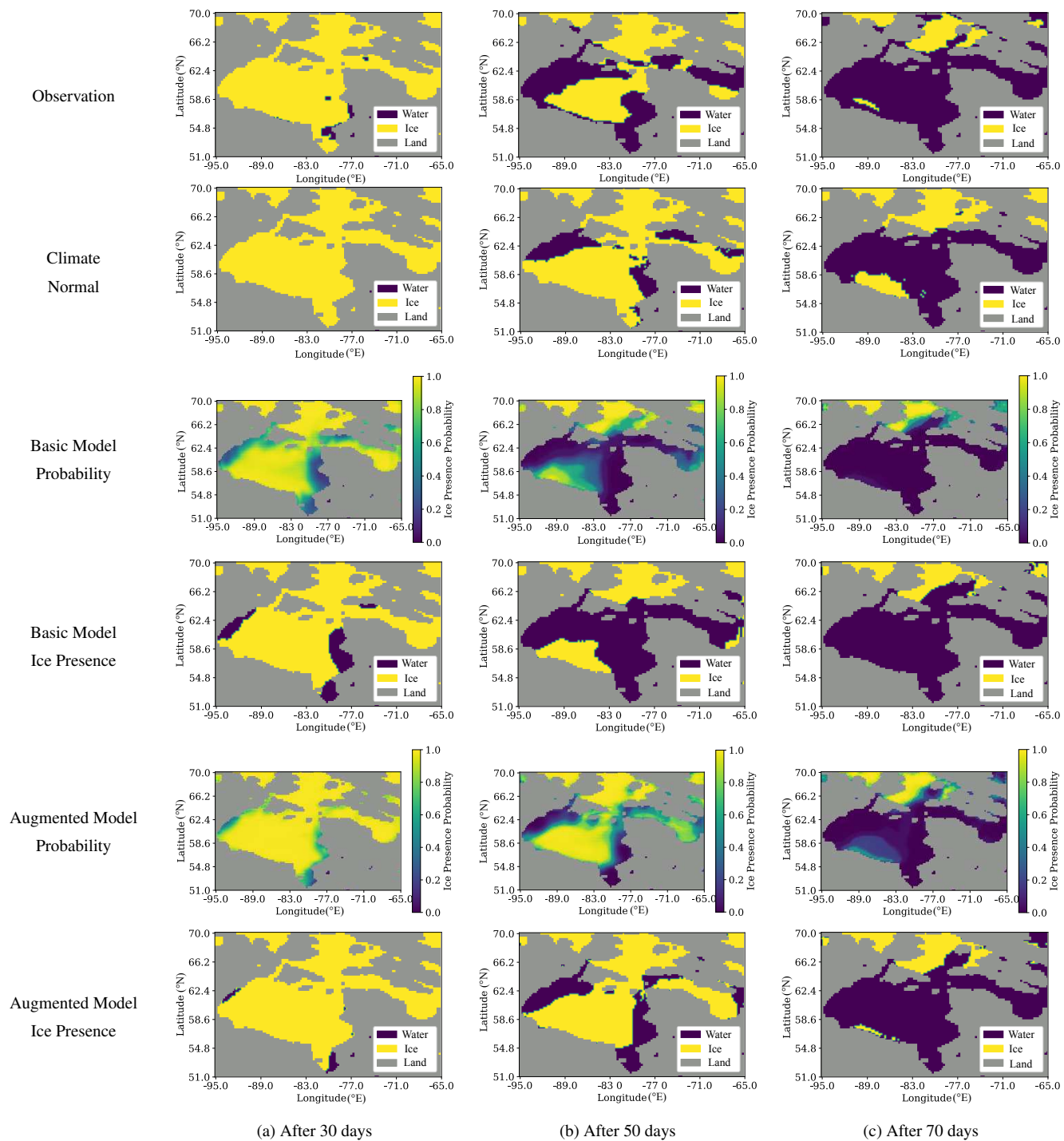
Figure 7. Spatial patterns of sea ice presence during break-up. These models are trained using data from May, June, and July. The forecasts are launched on May, 6th, 2014 and are displayed after 30 days (June 5th), 50 days (June 25th) and 70 days (July 15th).

(a)Climate Normal (b)Basic Model (30 lead day) (c)Basic Model (60 lead day)

(d)Augmented Model (30 lead day) (e)Augmented Model (60 lead day)
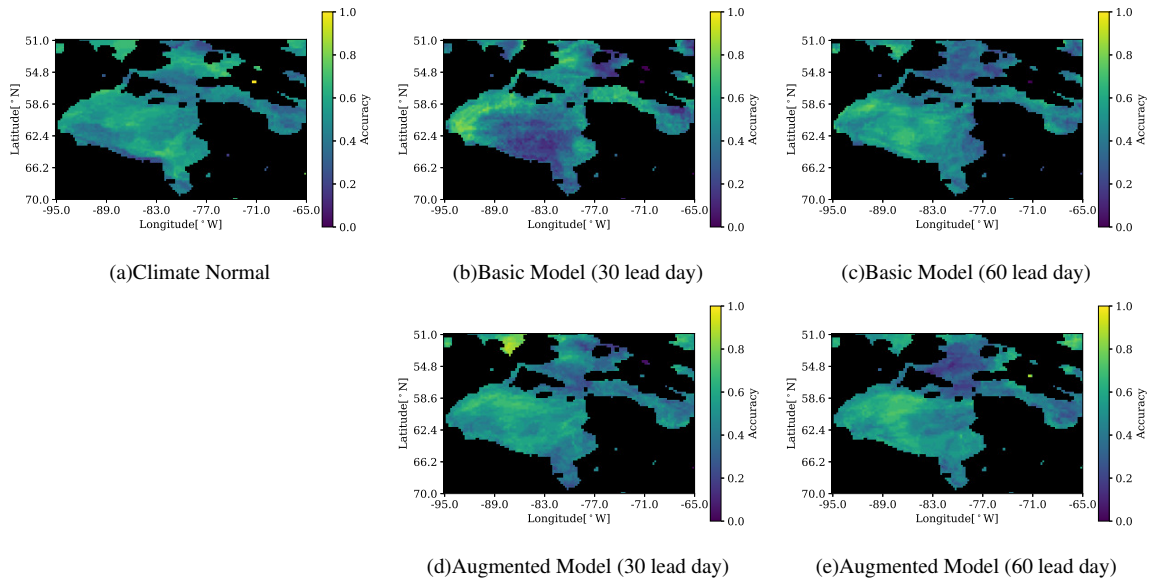
Figure 8. Accuracy of predicted freeze-up date within 7 days. Freeze-up dates are checked from October 1st to January 31st. The 7-day window is chosen to match to definition used by the Canadian Ice Service.

the predicted and observed freeze-up/break-up dates per pixel per year are compared. If the 2 dates are within 7 days of each other, the prediction is correct (a value of one is assigned), and if not the prediction is in incorrect (a value of zero is assigned). Then, the results are averaged over the total number of years to obtain an overall score between 0 and 1, which we will refer to as freeze-up/break-up accuracy.

7.2.2   Freeze-up and Break-up in comparison with ERA5 data

We start our comparison using ERA5 as the baseline, consistent with our earlier comparisons. Figure 8 and 9 show the freeze-up and break-up accuracy maps of the Climate Normal as well as the Basic and Augmented model for 30 and 60 lead days The freeze-up accuracy maps (Fig 8) show similar spatial patterns for the Basic and Augmented models, with the exception of the Basic model at 30 lead days (Fig 9b). To investigate the prediction of freeze-up by the Basic model at 30 lead days, we looked at model forecasts from the November and October models for 30 and 60 lead day respectively, as freeze-up mainly happens in December. It was found (not shown) that the December sea ice presence accuracy of the Basic model at lead day 30 is lower in the central region and higher in Hudson Strait compared to other methods, which explains the difference in freeze-up prediction maps. The poorer accuracy in the central region was because freeze-up was too late, discussed further in Section 9.

In contrast to freeze-up, for the break-up accuracy (Fig. 9) the Climate Normal (Fig 9a) has an overall poor accuracy, while the Augmented model at 30 lead days (Fig 9d) has the best accuracy, especially in the central region. The break-up prediction accuracy degrades at 60 lead days for both the Basic and Augmented models.
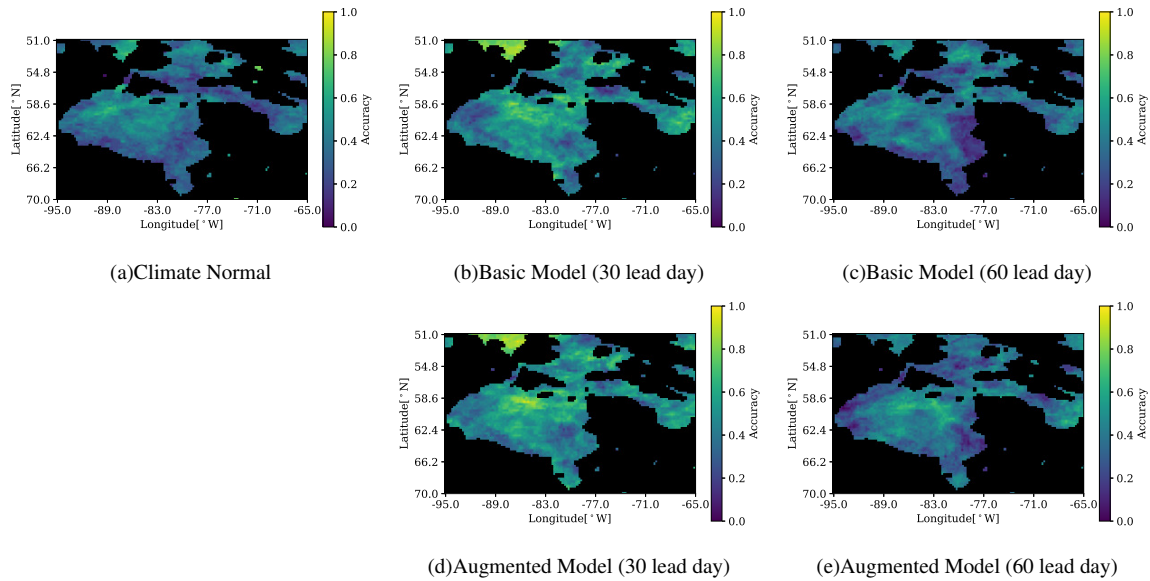
Figure 9. Accuracy of predicted break-up date within 7 days. Break-up dates are checked from May 1st to July 31st. The 7-day window is chosen to match to definition used by the Canadian Ice Service.

The interannual variability of accuracy in freeze-up (October 1st to January 31st) and break-up (May 1st to July 31st) predictions is presented in Fig 10 for 30 and 60 lead days. The respective trends are shown by dashed lines. While no significant trend is observed for freeze-up accuracy at both lead times, the break-up accuracy ((c) and (d)) shows a declining trend of 2%. Similar to Fig 9 for freeze-up/break-up date predictions, both the Augmented and Basic models have their highest improvement compared to Climate Normal for break-up at 30 lead days. In addition, for both cases, 2010 shows an extreme case where Climate Normal has the lowest accuracy over the entire period. For that year, the Augmented model has a lower freeze-up accuracy compared to other years, while its break-up accuracy does not show any significant variability over the years. It has been noted in an earlier study that 2010 was an anomalous year (Hochheim and Barber, 2014).

The ability of the model to predict freeze-up and break-up dates can provide helpful information for local communities and shipping operators. Here, the nearest pixels to three sample ports shown in Fig 1, Churchill, Inukjuak, and Quaqtaq, and Sanirajak (formerly known as Hall Beach) are selected. The sites were chosen because they represent locations with significantly different sea ice conditions. Churchill and Inukjuak are located on the east and west coasts of Hudson Bay, with Churchill being a major port as part of the potential Arctic Bridge shipping route. The east coast is significantly impacted by influx of freshwater inflow from rivers draining into Hudson Bay, while the west coast region is impacted by northwesterly winds (there is a latent heat polynya, the Kivalliq polynya, that runs along the northwest shore of Hudson Bay (Bruneau et al., 2021)). There are additionally east-west asymmetries in Hudson Bay in terms of ice thickness and sea surface temperature (Saucier, 2014), with counter-clockwise ocean currents leading to thicker ice covers along the eastern shore of the bay. Quataq
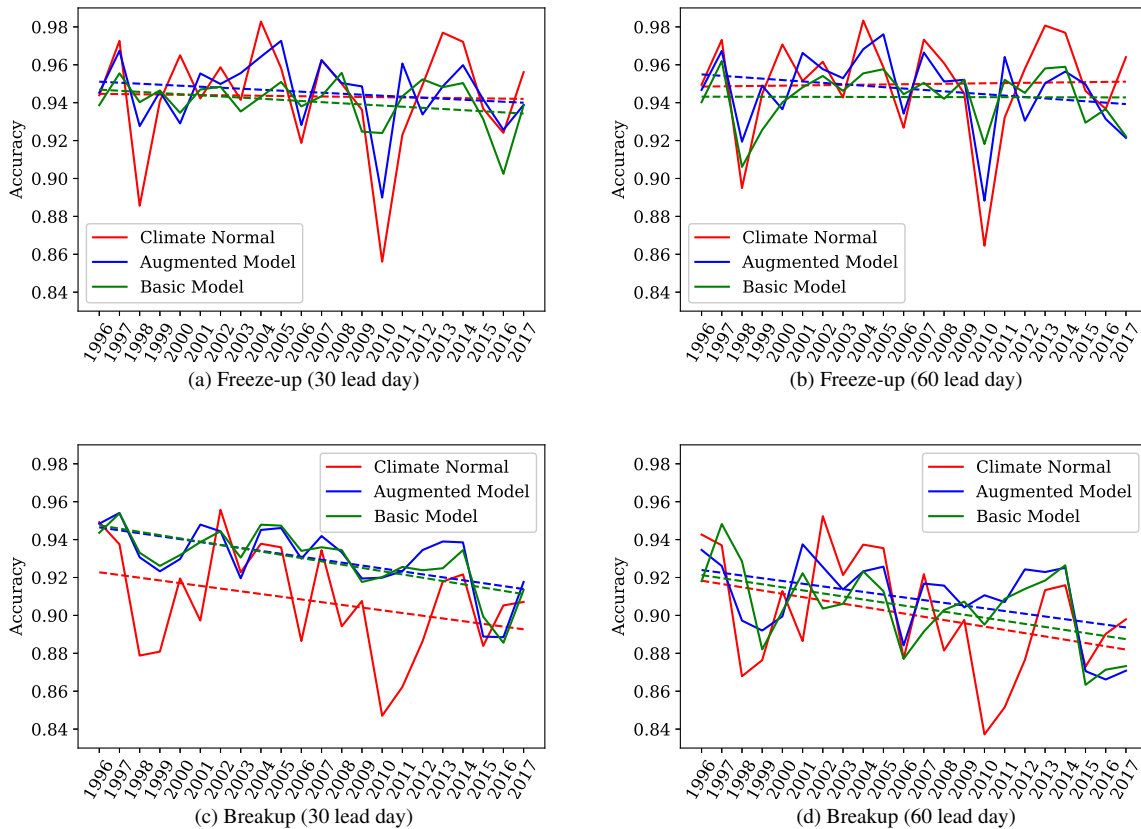
Figure 10. Accuracy of the Climate Normal, Basic model and Augmented model freeze-up and break-up predictions over the years at 30 and 60 lead day. Dashed lines show the trend.

is located in Hudson strait, where wind and air temperature patterns are different from those in Hudson Bay, and pressured ice is common.

Freeze-up/break-up date predictions of the models at 30 and 60 lead day versus observed dates are presented in Figures 11 and 12. The red line in each plot represents a perfect one-to-one prediction and the pink region shows the acceptable 7 days difference that will still be considered as a correct prediction according to the CIS criteria. The width of the pink zone on each plot varies as the total time frame of break-up and freeze-up at each location is different (i.e. the subplots have different x and y axes). In addition, the year of 2010 is omitted from these plots as it was an anomalously warm year (Hochheim and Barber, 2014).

For freeze-up, 30 lead day predictions are more concentrated and closer to the pink zone while there is more dispersion and outliers observed for 60 lead day predictions (Fig 11). In addition, Augmented model predictions have fewer outliers than Basic model predictions. For the port of Churchill, predictions are close to the center and inside or close to the pink zone for both models and both lead times compared to other locations. The Basic model especially at 30 lead day, predicts freeze-up

dates of several years with a consistent delay for Inukjuak while for Quaqtaq its predictions are earlier than observed dates. In Fig 12, similar to freeze-up, break-up dates are better captured by Augmented model at 30 lead days as compared to 60 lead days, where predictions are more scattered. Also, the patterns of early and delayed predictions are not as visible as for break-up as for freeze-up for Inukjuak and Quaqtaq ports.

7.2.3 Comparison with operational ice charts

To assess the operational capability of the models (Table 1), it is important to consider the authoritative source of information used by shipping operators as a baseline for comparison. Observed freeze-up and break-up dates were extracted from the Canadian Ice Service (CIS) regional ice charts using the same methodology described section in 7.2.1. The use of CIS daily ice charts was discarded due to non-standardized spatiotemporal coverage and data availability to conduct this analysis from 1996 to 2016. It is important to note that the CIS regional ice charts are produced on a weekly or biweekly basis and therefore provide freeze-up and break-up dates at a fairly coarse temporal resolution compared to the needs of this assessment. CIS charts are compiled through a manual assimilation of data from synthetic aperture radar imagery, sea ice concentration from passive microwave data, optical data and ship reports. The analysis using CIS charts complements the break-up and freeze-up dates derived from ERA-5 daily ice concentration as a second baseline for model evaluation.

Three sites were selected for this assessment: Kivalliq polynya near Arviat port (61.19N, 93.49W), Kinngait (64.05N, 76.48W) and Sanirajak (68.83N, 81.10W). These sites were selected because each is near a port location, and each is also associated with a polynya, and therefore the ice cover is challenging to predict. The accuracy of freeze-up and break-up dates at each site was evaluated against both CIS regional ice charts and ERA-5 baselines. The predictions of the Basic and Augmented models at 30 and 60 lead days were assessed using 2 metrics: Mean Absolute Error (MAE) and Accuracy within 7 days. Forecasts using median break-up and freeze-up dates derived from CIS regional ice charts from 1980 to 2010 and published in the Canadian Ice Service's Ice Atlas 1980-2010 (CIS, 2013) are also evaluated using the same methodology. For the Sanirajak site, each time break-up was outside the date range defined by the extraction methodology (May 1st to July 31st) from the ERA5 baseline or model forecast, the missing date was replaced by the ice atlas freeze-up date, October 22nd, in order to calculate both metrics.

For break-up, at the Kivalliq site, the 30 day Augmented model showed the best performance based on MAE and accuracy metrics using ERA5 baseline, while the Basic model at 30 lead days tends to perform better using CIS ice charts as baseline. The break-up dates for the Kinngait site show higher interannual variability, suggested by the poor performance of the ice atlas using both baselines. The break-up forecast skill is relatively consistent for both Basic and Augmented models at 30 and 60 lead days, but show higher skill for all models and ice atlas using the ERA5 baseline compared to CIS ice charts. The difference in break-up dates derived from the two baselines is significant at this site (Table 2), where events such as early break-up in March 2012 are captured by the CIS ice charts but not by the ERA5 reanalysis. For Sanirajak site, the difference between baselines is exacerbated. The CIS regional ice charts, which rely on human analysts and synthetic aperture radar (SAR) imagery, consistently detect early break-up at the polynya site, while the ERA5 reanalysis does not, produced from low resolution passive microwave instruments. As a result, the majority of break-up dates derived from ice charts were before
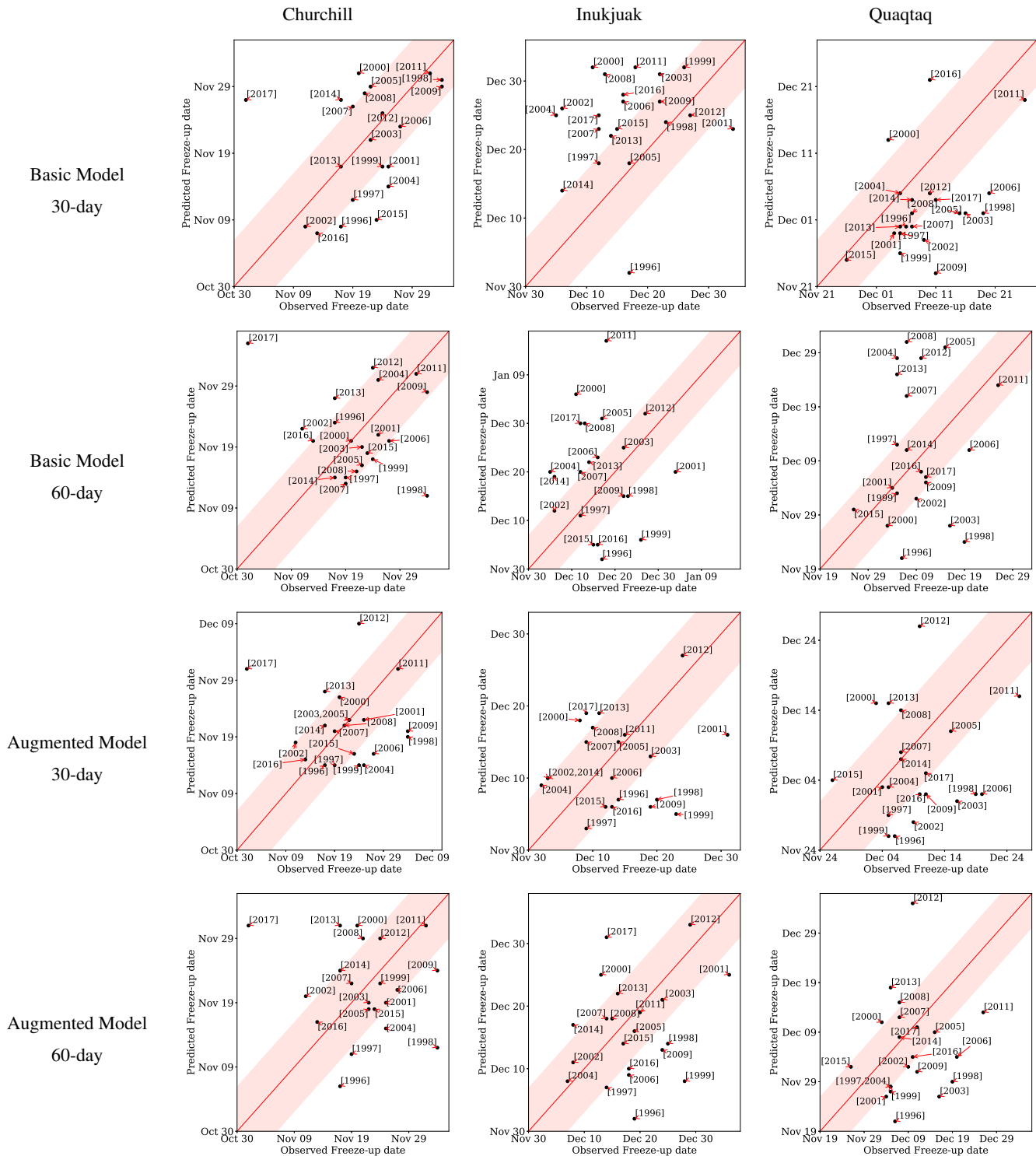
Figure 11. Comparison between forecast and observed freeze-up dates at pixels located in the vicinity of ports in the study region for 30 lead days and 60 lead days. Each dot represents one year. The red line represents perfect predictions and the pink area represents +/- 7 days of the red line, which is commonly assumed as an acceptable error range. **17**
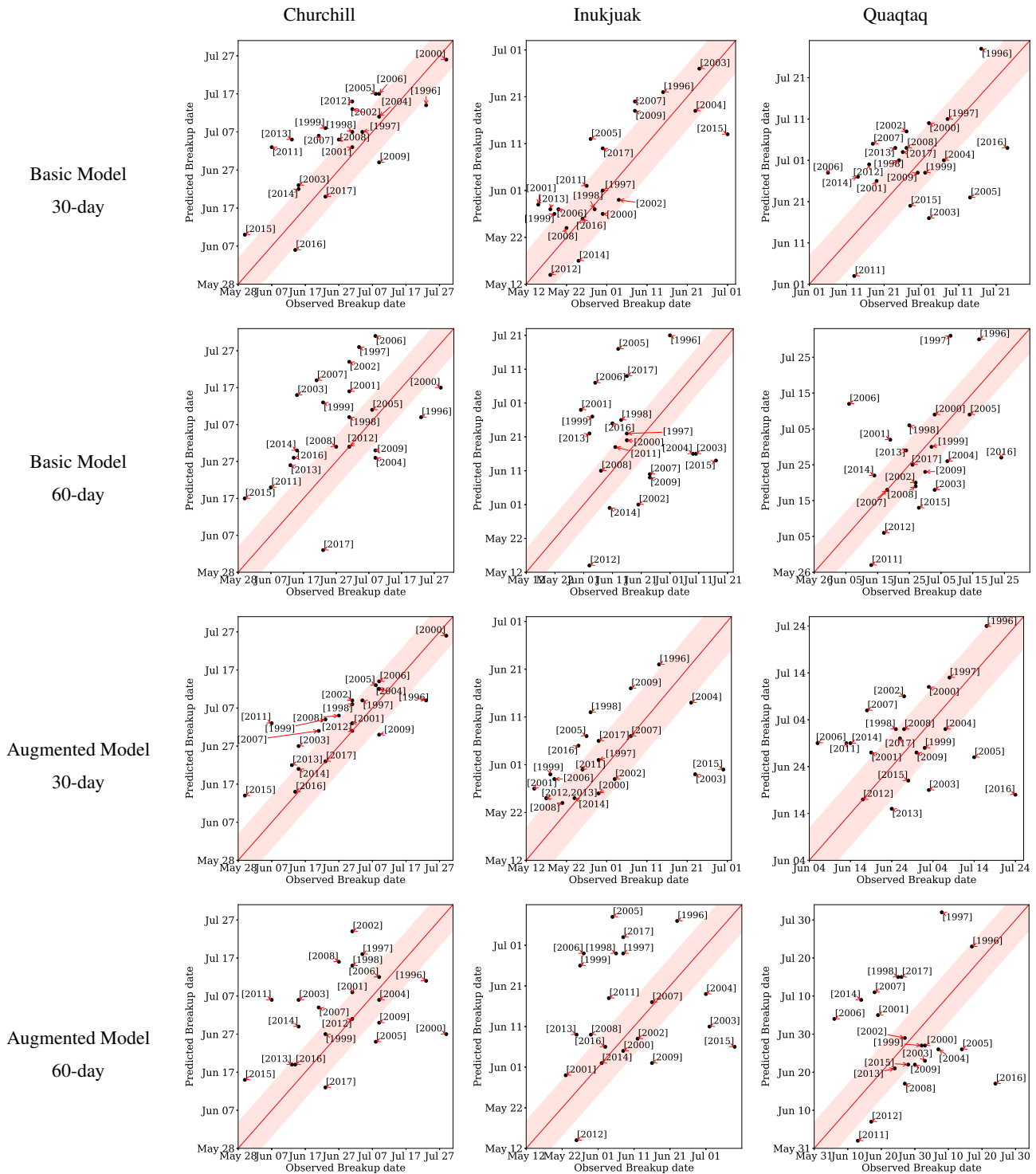
Figure 12. Comparison between forecast and observed break-up dates at pixels located in the vicinity of ports in the study region for 30 lead days and 60 lead days. Each dot represents one year. The red line represents perfect predictions and the pink area represents +/- 7 days of the red line, which is commonly assumed as an acceptable error range.

Area	Baseline	Breakup Mean Absolute Error (days)					Breakup Accuracy				
		Basic 30	Augmented 30	Basic 60	Augmented 60	Ice Atlas	Basic 30	Augmented 30	Basic 60	Augmented 60	Ice Atlas
Kivalliq	ERA5	14.10	12.38	13.67	18.14	15.52	0.29	0.48	0.38	0.10	0.43
Kinngait	ERA5	13.05	13.14	17.00	13.81	17.71	0.14	0.29	0.38	0.24	0.29
Sanirajak	ERA5	25.19	24.24	20.76	17.52	87.33	0.43	0.48	0.38	0.48	0.00
Kivalliq	Ice Chart	10.10	13.52	14.52	15.57	13.90	0.43	0.19	0.29	0.19	0.29
Kinngait	Ice Chart	25.76	25.86	28.95	25.57	34.62	0.05	0.05	0.10	0.14	0.05
Sanirajak	Ice Chart	90.90	97.95	86.67	82.48	18.67	0.05	0.05	0.05	0.00	0.43
Area	Baseline	Freeze-up Mean Absolute Error (days)					Freeze-up Accuracy				
		Basic 30	Augmented 30	Basic 60	Augmented 60	Ice Atlas	Basic 30	Augmented 30	Basic 60	Augmented 60	Ice Atlas
Kivalliq	ERA5	6.05	7.71	5.81	7.95	5.33	0.62	0.52	0.71	0.52	0.71
Kinngait	ERA5	7.48	12.38	11.00	13.33	8.10	0.62	0.43	0.38	0.33	0.71
Sanirajak	ERA5	9.10	6.48	9.86	8.52	8.14	0.43	0.67	0.43	0.52	0.52
Kivalliq	Ice Chart	8.90	9.90	9.81	10.81	7.81	0.48	0.52	0.43	0.52	0.62
Kinngait	Ice Chart	13.90	19.67	18.10	20.43	13.76	0.43	0.33	0.29	0.33	0.52
Sanirajak	Ice Chart	10.33	15.52	15.67	17.00	9.86	0.43	0.33	0.29	0.24	0.43

Table 1: Break-up and freeze-up forecast accuracy at selected sites of the CIS Ice Atlas, Basic and Augmented model at 30 lead day and 60 lead day versus baseline observations derived from CIS regional ice charts and ERA5

July 1st, whereas this occurs only once in 2016 using the ERA5 baseline. The baseline discrepancy explains why Basic and Augmented models performed better using ERA5 baseline, while the ice atlas has better skill using the CIS ice chart baseline. However, both have similar skill using their corresponding baseline. Part of the discrepancy between the scores using ERA5 as a baseline in comparison to the ice charts at this location is because for the Basic and Augmented models, forecasts initialized up to July 31st were considered, which means late break-up dates were missing in the time window (up to Aug 30th for a 30 day forecast, and up the Sept 30th for a 60 day forecast and ERA5 baseline) and were replaced by the ice atlas freeze-up date, October 22nd, in order to calculate both metrics. Only forecasts at the Sanirajak location are impacted by this because at other sites break-up occurred before July 31st for both the Basic and Augmented model.

The performance forecasting freeze-up is very high for all models at the Kivalliq site, with the lowest freeze-up accuracy at 0.52 using ERA5 baseline or 0.43 using CIS ice charts baseline. For all sites, the ice atlas showed the highest freeze-up forecasting skill against both baselines, due to the lower interannual variability in freeze-up dates compared to break-up dates. These results are consistent with the freeze-up and break-up accuracy maps (Figs 8 and 9).

Table 2 highlights the discrepancy between the two baselines using the same metrics as Table 1, where MAE can be interpreted as Mean Absolute Difference between the two baselines and the accuracy can be interpreted as the fraction of the time the baseline dates are within 7 days of each other. As expected, there is a minimal discrepancy for large and uniform areas such as the Kivalliq site, explained by the weekly publication frequency of the CIS regional ice charts. The discrepancy is higher for smaller and localized polynyas, such as the Kinngait and Sanirajak sites, where the low resolution passive microwave instruments used by ERA5 do not detect them compared to CIS regional ice charts.

8 Comparison with forecast data from ECMWF S2S system

To evaluate our approach further we have carried out a comparison between our model forecasts and those from the subseasonal-to-seasonal (S2S) system by ECMWF (Vitart and Robertson, 2018). The S2S predictions are launched twice a week (Monday

and Thursday), with forecasts for lead times up to 46 days. For the comparison presented here, the data from our system (Basic model, Augmented model, Climate Normal and observations) are extracted for the same launch dates as those used for the S2S system. The S2S data was extracted at a spatial resolution of $0.25^o \times 0.25^o$, and interpolated to our 31 km grid resolution using a nearest neighbour approach. The binary accuracy is calculated as described in Section 6. Results are shown only for 2016 and 2017 because these are the years for which forecasts are available for the S2S system that overlap with our study period. Results are shown only for forecasts launched during months for which there are notable differences between the methods, which are May-June and October-November.

Binary accuracies are shown as a function of lead day for 2016 and 2017 in Fig 13. During May and June both the Basic and Augmented models have a higher binary accuracy than the S2S forecasts, while during October and November the opposite behaviour is observed, with the Basic and Augmented models having similarly low accuracies. We investigate these differences below using false positive and false negative rates. The false positive rate is $FP_{rate} = FP/(FP+TN)$ and is the ratio of incorrectly classified water points in the domain (false positives, FP) to total water points $(FP+TN)$, where TN is the true negatives, or number of correctly classified water points. The false negative rate is $FN_{rate} = FN/(FN+TP)$, and is the ratio of incorrectly classified ice points in the domain (false negative, FN) to the total number of ice points $(FN+TP)$, where TP is the true positives, or number of correctly classified ice points.

In Fig 14 spatial maps showing the binary accuracy, false positive rates and false negative rates, for forecasts at lead day 30 launched on dates between June 1st and June 30th are shown. These forecasts correspond to ice conditions from July 1 to July 30th. The white regions correspond to locations masked out due to land, or where are are no positives (ice points) in the false positive plots, and similarly in the false negative plots. For example, there is no ice in the northwest portion of the domain at this time of the year. For the Basic and Augmented models there is a high false positive rate in the south-east portion of Hudson Bay, indicating the sea ice is not retreating fast enough relative to the observations. However, for the S2S forecasts the false positive rate is high over almost all of Hudson Bay, including Hudson Strait. Climate Normal has the lowest false positive rate of the approaches examined here. For the false negative rate, different behaviour is observed with a high false negative rate for Climate Normal, indicating too much open water, and slightly lower false negative rates for the Basic and Augmented models. The Augmented model has a higher false negative rate that the Basic model, suggesting some of the overprediction of open water may be related to the additional air temperature or windspeed data that are input to this model. The strong recovery of the binary accuracy of the S2S forecasts around day 35 (Fig 13b) is due to the ice quickly retreating in these forecasts (not shown).

| | Discrepancy ERA5 - Ice Charts | | | |
| | Break-up | | Freeze-up | |
	MAE	Accuracy	MAE	Accuracy
Kivalliq	8.76	0.48	5.81	0.76
Kinngait	18.52	0.38	8.14	0.67
Sanirajak	85.52	0.10	11.33	0.48

Table 2: Discrepancy between break-up and freeze-up dates derived from ERA5 and CIS regional ice charts.
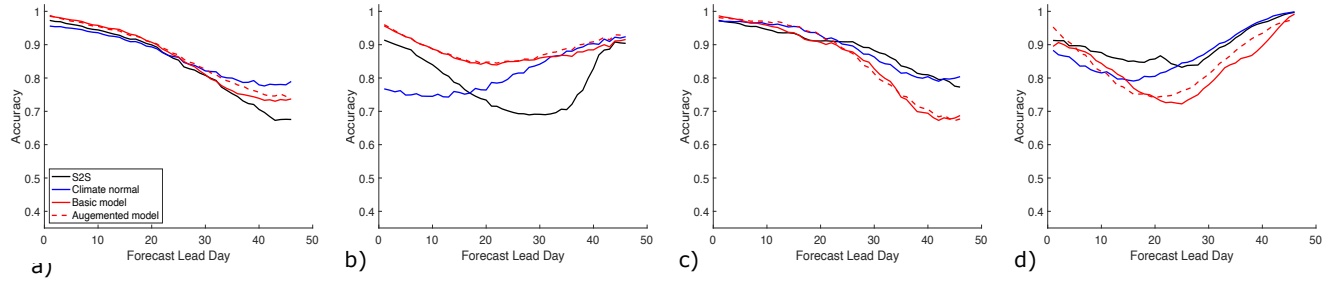
Figure 13. Binary accuracy as a function of lead day for forecasts launched in a) May; b) June; c) October; d) November. These months were chosen because they display the largest differences between the various forecasting methods Binary accuracies are evaluated using data from both 2016 and 2017. .
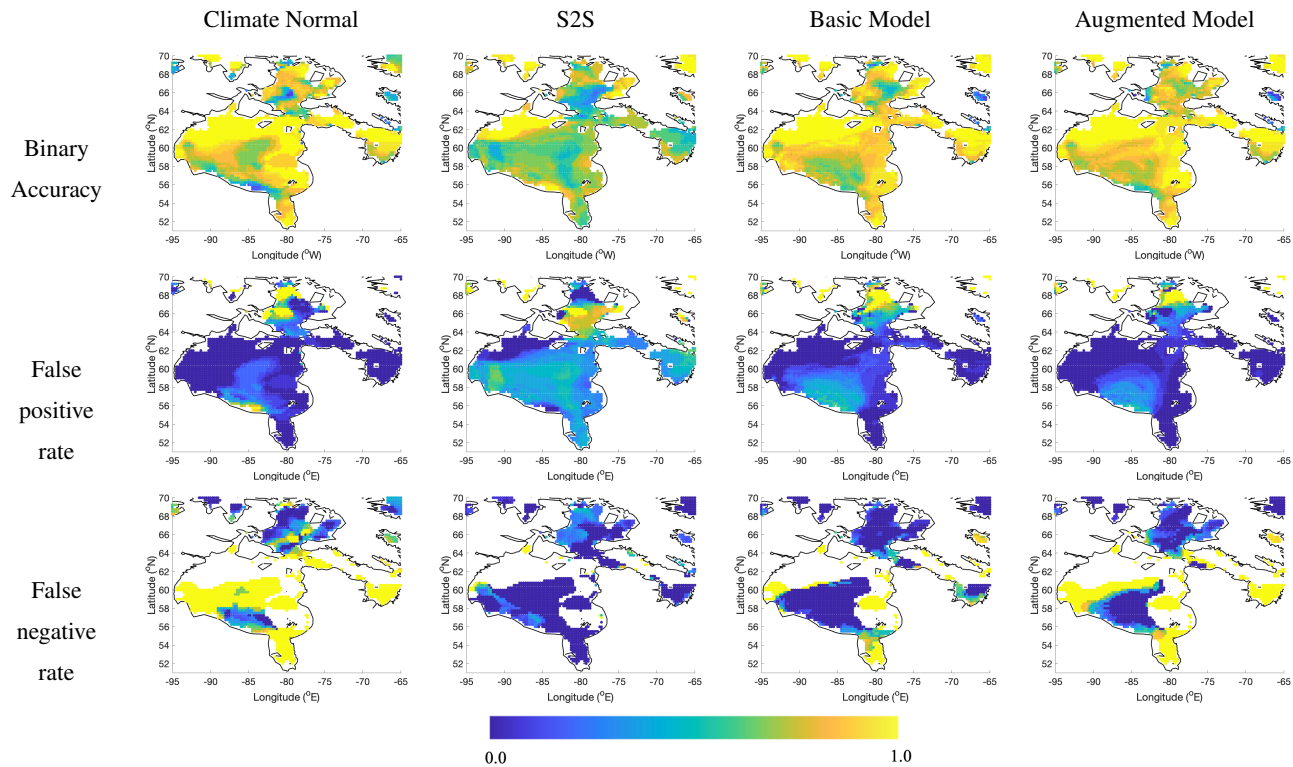
Figure 14. Comparison of forecasting approaches for June at 30 lead days.
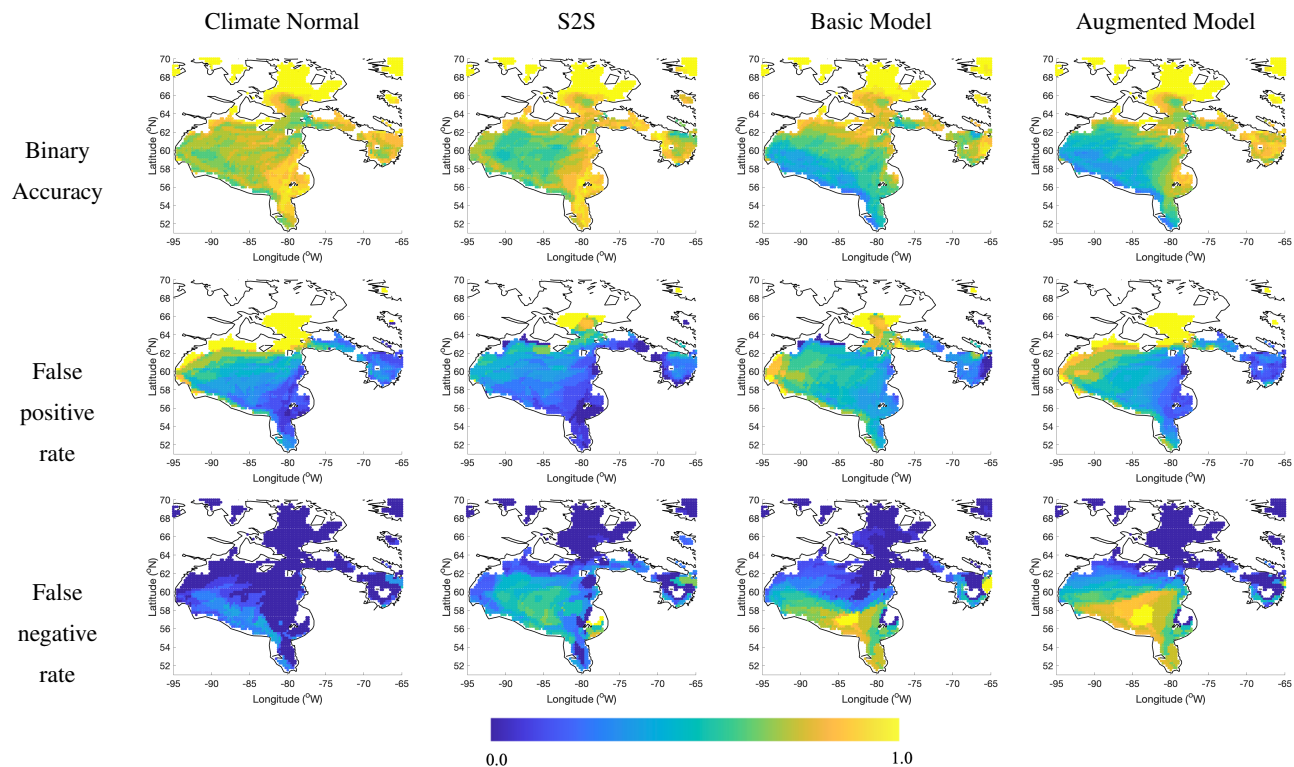
Figure 15. Comparison of forecasting approaches for October at 45 lead days.

During October and November the S2S forecasts have a much higher binary accuracy than those from the proposed approach (Fig 13 panels c, d). The poor performance of the Basic and Augmented model is in part due to the opening of the Kivalliq

385 polynya (Bruneau et al., 2021) in the northwestern portion of the domain (Fig 15, false positive rates). This is a large latent heat polynya that is sustained in part due to strong offshore winds. The Basic model, Augmented model and Climate Normal all predict freeze-up too quickly in this region, in comparison to the observations, while the S2S forecasts are able to represent this better (false positive rates, Fig 15). The superior performance of the S2S forecasts may be because the S2S system uses a prognostic sea ice model coupled to the atmosphere. When ice starts to form this reduces the heat exchange from the ocean to

390 the atmosphere, and the rate of ice growth slows. The proposed approach may have had trouble representing this phenomena because the patterns learned associated with the variables used for training.

9 Discussion

The proposed spatial-temporal sea ice forecasting method is capable of predicting sea ice presence probabilities with skill during May, June and July (break-up) in comparison to both Climate Normal and sea ice concentration forecasts from a leading

395 S2S system. Results during freeze-up are more mixed, with an indication of higher accuracy in November in comparison to

Climate Normal at early lead times (Fig 1d), but degradation at longer lead times, and larger discrepancies with S2S forecasts. Regarding the poor performance of the Basic model in predicting freeze-up at 30 lead days (Fig 8b) vs 60 lead days (Fig 8c), we note the freeze-up criteria is checked for dates between October 1st and January 31st. For this range of dates, 30-day forecasts would have been launched between September 1st and December 31st, and the models would have been trained on data from August 1st to October 31st (for the September model) and November 1st to January 31st (for the December model). In contrast, 60-day forecasts would have been launched one month earlier, and trained on data covering the same three month span, but starting one month earlier. We hypothesize the 60 day forecasts are better than the 30 day forecasts because the air temperature can have more of an impact for 60 day forecasts as the open water season is considered more heavily in the training data for the 60 day model (training data extends into July). Hochheim and Barber (2014) note a dependence of sea ice extent on air temperatures during freeze-up in this central region of Hudson Bay. The additional inputs to the Augmented model, which includes air temperature and the wind components, may account for the improved performance of the Augmented model in comparison to the Basic model for this scenario.

Throughout the paper the Basic and Augmented models have been compared. While the Augmented model was not developed to address a specific problem with the Basic model, it was developed to enforce a climate normal, which can help the model generalize, meaning produce better forecasts over a wider range of conditions. It was found (Fig 4f and trend lines in Fig 10) the Augmented model generally has higher accuracy than the Basic model. The comparison with the S2S forecasts and Climate Normal, shown in Fig 13 and 14, indicate these two approaches are in better agreement with each other than the S2S forecasts, with the Augmented model in closer agreement with Climate Normal that the Basic model, as expected.

It is worthwhile to consider how our results compare with those of similar studies in the region. Gignac et al (2019) and Dirkson et al (2019) developed methods for probabilistic forecasting based on fitting probability distribution functions (PDFs) to historical passive microwave sea ice concentration data. Gignac et al (2019) in particular focused on the same geographic region as the present study, choosing a beta PDF to fit the data and define a model from which they could query the probability of ice, given a date. Following the same definition of break-up and freeze-up as used here, they found their approach was able to capture freeze-up and break-up within one or two weeks of dates provided by the Canadian Ice Service (CIS) ice atlas, with the exception of Sanirajak (formerly known as Hall Beach), similar to the results reported here. Their discrepancy was 9 weeks (or 63 days), hence slightly shorter than ours (Table 1), although we have used ice charts directly, while they type of climatology based on ice charts. They related this discrepancy to the use of a mean when processing the passive microwave data, in comparison the the median used for the ice atlas. We agree this could. be a contributing factor, but also not the passive microwave data are biased when the ice is thin (as is the case in a polynya) Ivanova et al. (2015). Dirkson et al (2019) developed a related approach but used zero and one inflated beta distribution to allow the endpoints of their probability distribution to be captured differently than the interior points. Their PDF is fit to data from a prognostic modelling system, CanSIPS, (Canadian Seasonal to Interannual Prediction System), which consists of two coupled atmosphere-ice-ocean models and a bias correction approach is applied to their predictions and CanSIPS output before comparison with HadISST2 sea ice and surface temperature dataset. Their predictions show skill in Hudson Bay for forecasts initialized in May and June for 1-2 months (their Fig 10), but

little skill for freeze-up, similar to what is found in the present study. Studies using coupled ice-ocean models (Sigmond et al., 2016; Bushuk et al., 2017) show more skill for freeze-up than break-up, consistent with the S2S results found here.

10   Conclusion

This study has focused on sea ice presence probability forecasting using deep learning methods at a daily time scale with lead times up to 90 days in advance. The Basic model uses eight input variables from the ERA5 dataset over the last 3 days before the initial date on which the forecast is launched. An augmented version of this basic model is also proposed where it takes an additional input from climate variables over the forecasting period. Comparing the binary accuracy of the Basic and Augmented models and Climate Normal demonstrated improvements of up to 10% relative to climate normal for both the break-up and freeze-up seasons, especially for early lead days (up to 30 days). The probability assessment by the calibration analysis and Brier score also revealed most differences in break-up and freeze-up season with scores from Augmented model slightly better in comparison to the Basic model. The analysis of break-up and freeze-up date prediction of the models shows the Augmented model is more capable at accurately predicting these dates within 7 days compared to the Basic model while the accuracy of both models degrades with increasing lead day. It should be noted that both models have substantial improvement over Climate Normal at 30 lead day for break-up date prediction.

Compared to operational forecasting systems in this domain, the proposed approach has the advantage of time efficiency as once the initial model is trained, the fine-tuning process for new inputs (consisting of one year of training data) takes around 15 minutes on a Tesla GPU and each inference takes around 10 seconds to complete. We also do not envision it to be difficult to use our approach with alternate input data from the point of view of model architecture. We recommend that if one was to use input data from a different reanalysis that they fine-tune the existing weights to account for the different data dependencies in the input data (in particular consider that only a subset of model variables are used, dependences present in one subset may be partially considered in a different subset for a different model). Finally, while the model here is demonstrated in hindcasting mode, it can (and is intended) to be used in forecast mode where, given an input time series of three days, forecasts can be generated up to 90 days lead time.

A limitation of our approach is that it relies on data from reanalyses. Without an additional downscaling module, the spatial resolution of our forecasts cannot exceed that of the input data, which here is 31 km. We note this resolution is similar to that used in other studies on seasonal forecasting that have been developed with mariners in mind. For example, passive microwave data were used for development of the probabilistic approach of Gignac et al. (2019) and for validation of subseasonal-to-seasonal sea ice predictions (Zampieri et al. 2018). While passive microwave sea ice concentration data are often gridded to 25 km, the spatial resolutions of the brightness temperature data used to generate the sea ice concentration are typically coarser. The 19.35 GHz channel on the SSMI and SSMI/S sensors (often used to produce sea ice concentration observations) has an instrument field of view of approximately 45 km x 69 km. For studies that carry out seasonal forecasting using a dynamic ice-ocean model (or similar) where a sea ice state vector is predicted as a function of time, our resolution is similar to that used in other approaches to be used to support (in part) marine transportation (Sigmond et al., 2016, Askenov et al 2017).

As future work, we plan to expand the experiments over the entire Arctic region, and deploy ensemble methods using more recent deep learning architectures. Looking into possible improvements by adding SIC anomaly as additional input variable as
465 investigated by Kim et al. (2020) is another path to explore.

Author contributions. PL, MK and MR designed and initiated the study and proposed the model. NA designed the experimental setup and performed the simulations and analysis of the results. PL and KAS supervised the study and provided feedback. NA, PL, MK, and KAS contributed to the development and writing of this paper.

Competing interests. The authors declare that they have no conflict of interest.

470 *Acknowledgements.* The authors would like to acknowledge funding from the National Research Council of Canada through the AI4Logistics and Ocean Programs and computing resources provided by Compute Canada.

References

Andersson, T. R., Hosking, J. S., Pérez-Ortiz, M., Paige, B., Elliott, A., Russell, C., Law, S., Jones, D. C., Wilkinson, J., Phillips, T., et al.: Seasonal Arctic sea ice forecasting with probabilistic deep learning, Nature Communications, 12, 2021.

475 Andrews, J., Babb, D., Barber, D. G., and Ackley, S. F.: Climate change and sea ice: shipping in Hudson Bay, Hudson Strait, and Foxe Basin (1980–2016), Elementa: Science of the Anthropocene, 6, 2018.

Askenov, Y., Popova, E., Yool, A., Nurser, A., Williams, T., Bertino, L., and Bergh, J.: On the future navigability of Arctic sea ice routes: High-resolution projections of the Arctic Ocean and sea ice, Marine Policy, 75, 300–317, 2017.

Bruneau, J., Babb, D., Chan, W., Kirillov, S., Ehn, J., Hanesiak, J., and Barber, D.: The ice factory of Hudson Bay: Spatiotemporal variability
480 of the Kivalliq polynya, Elementa Science of the Anthropocene, 9, 2021.

Bushuk, M., Msadek, R., Winton, M., Vecchi, G., Gudget, R., Rosati, A., and Yang, X.: Skillful regional prediction of Arctic sea ice on seasonal time scales, Geophysical Research Letters, 44, 10.1022/2017/GL073 155, 2017.

Carrieres, T., Buehner, M., Lemieux, J.-F., and Pedersen, L., eds.: Sea ice analysis and forecasting : towards an increased resilience on automated prediction system, Cambridge University Press, 2017.

485 Chevallier, M., Salas y Mélia, D., Voldoire, A., and Deque, M.: Seasonal forecasts of pan-Arctic sea ice extent using a GCM-based seasonal prediction system, Journal of Climate, 26, 6092–6104, 2013.

Chiu, C.-C., Sainath, T. N., Wu, Y., Prabhavalkar, R., Nguyen, P., Chen, Z., Kannan, A., Weiss, R. J., Rao, K., Gonina, E., et al.: State-of-the-art speech recognition with sequence-to-sequence models, in: 2018 IEEE International Conference on Acoustics, Speech and Signal Processing (ICASSP), pp. 4774–4778, IEEE, 2018.

490 Cho, K., Van Merriënboer, B., Gulcehre, C., Bahdanau, D., Bougares, F., Schwenk, H., and Bengio, Y.: Learning phrase representations using RNN encoder-decoder for statistical machine translation, in: Empiricial Methods in Natural Language Processing EMNLP, pp. 1724–1734, 2014.

CIS: CIS: Sea Ice Climatic Atlas for the Northern Canadian Waters 1981–2010, Canadian Ice Service (CIS), Ottawa, 2013.

Drobot, S., Maslanik, J., and Fowler, C.: A long-range forecast of Arctic summer sea-ice minimum extent, Geophysical Research Letters,
495 33, L10 501, 2006.

Dupont, F., Higginson, S., Bourdallé-Badie, R., Lu, Y., Roy, F., Smith, G. C., Lemieux, J.-F., Garric, G., and Davidson, F.: A high-resolution ocean and sea-ice modelling system for the Arctic and North Atlantic oceans, Geoscientific Model Development, 8, 1577–1594, https://doi.org/10.5194/gmd-8-1577-2015, 2015.

Ferro, C. A.: Comparing probabilistic forecasting systems with the Brier score, Weather and Forecasting, 22, 1076–1088, 2007.

500 Fritzner, S., R., G., and Christensen, K.: Assessment of high resolution dynamical and machine learning models for prediction of sea ice concentration in a regional application, Journal of Geophysical Research, Oceans, 2020.

Guemas, V., Blanchard-Wrigglesworth, E., Chevallier, M., Day, J. J., Déqué, M., Doblas-Reyes, F. J., Fučkar, N. S., Germe, A., Hawkins, E., Keeley, S., et al.: A review on Arctic sea-ice predictability and prediction on seasonal to decadal time-scales, Quarterly Journal of the Royal Meteorological Society, 142, 546–561, 2016.

505 Hochheim, K. P. and Barber, D.: An update on the ice climatology of the Hudson Bay System, Arctic, Antarctic and Alpline Research, 46, 66–83, 2014.

Hochreiter, S. and Schmidhuber, J.: Long short-term memory, Neural computation, 9, 1735–1780, 1997.

Horvath, S., Stroeve, J., Rajagopalan, B., and Kleiber, W.: A Bayesian logistic regression for probabilistic forecasts of the minimum September Arctic sea ice cover, Earth and Space Science, 7, e2020EA001 176, 2020.

510 Howard, A. G., Zhu, M., Chen, B., Kalenichenko, D., Wang, W., Weyand, T., Andreetto, M., and Adam, H.: Mobilenets: Efficient convolutional neural networks for mobile vision applications, in: Computing Research Repository (CoRR) abs/1704.04861, 2017.

Ivanova, N., Pedersen, L. T., Tonboe, R. T., Kern, S., Heygster, G., Lavergne, T., Sørensen, A., Saldo, R., Dybkjær, G., Brucker, L., and Shokr, M.: Inter-comparison and evaluation of sea ice algorithms: towards further identification of challenges and optimal approach using passive microwave observations, The Cryosphere, 9, 1797–1817, https://doi.org/10.5194/tc-9-1797-2015, 2015.

515 Kim, Y., Kim, H.-C., Han, D., Lee, S., and Im, J.: Prediction of monthly Arctic sea ice concentrations using satellite and reanalysis data based on convolutional neural networks, The Cryosphere, 14, 1083–1104, 2020.

Lin, T.-Y., Dollár, P., Girshick, R., He, K., Hariharan, B., and Belongie, S.: Feature pyramid networks for object detection, in: Proceedings of the IEEE conference on computer vision and pattern recognition, pp. 2117–2125, 2017.

Melia, N., Haines, K., and Hawkins, E.: Sea ice decline and 21st century trans-Arctic shipping routes, Journal of Geophysical Research, 43, 520 9720–9728, 2016.

Sigmond, M., Fyfe, J., Flato, G., Kharin, V., and Merryfield, W.: Seasonal forecast skill of Arctic sea ice area in a dynamical forecast system, Geophysical Research Letters, 40, 529–534, 2013.

Sigmond, M., Reader, M., Flato, G., Merryfield, W., and Tivy, A.: Skillful seasonal forecasts of Arctic sea ice retreat and advance dates in a dynamical forecast system, Geophysical Research Letters, 43, 12–457, 2016.

525 Sutskever, I., Vinyals, O., and Le, Q. V.: Sequence to sequence learning with neural networks, in: Advances in neural information processing systems, pp. 3104–3112, 2014.

Tivy, A., Howell, S., Alt, B., Yackel, J., and Carrieres, T.: Origins and levels of seasonal skill for sea ice in Hudson Bay using canonical correlation analysis, Journal of Climate, 24, 1378–1394, 2011.

Tonboe, R., Eastwood, S., Lavergne, T., Sørensen, A., Rathmann, N., Dybkjaer, G., Pedersen, L., Høyer, J., and Kern, S.: The EUMETSAT 530 sea ice concentration climate data record, The Cryosphere, 10, 2016.

Venugopalan, S., Rohrbach, M., Donahue, J., Mooney, R., Darrell, T., and Saenko, K.: Sequence to sequence-video to text, in: Proceedings of the IEEE international conference on computer vision, pp. 4534–4542, 2015.

Vitart, F. and Robertson, A.: The sub-seasonal to seasonal prediction project (S2S) and the prediction of extreme events, njp Climate and Atmospheric Science, 1, 2018.

535 Wang, C., Graham, R., Wang, K., Gerland, S., and Granskog, M.: Comparison of ERA5 and ERA-Interim near surface air temperature, snowfall and precipitation over Arctic sea ice: effect on sea ice thermodynamics and evolution, The Cryosphere, 13, 1661–1679, 2019.

Xingjian, S., Chen, Z., Wang, H., Yeung, D.-Y., Wong, W.-K., and Woo, W.-c.: Convolutional LSTM network: A machine learning approach for precipitation nowcasting, in: Advances in neural information processing systems, pp. 802–810, 2015.

Yu, Y., Si, X., Hu, C., and Zhang, J.: A review of recurrent neural networks: LSTM cells and network architectures, Neural computation, 31, 540 1235–1270, 2019.

Zhang, J., Steele, M., Lindsay, R., Schweiger, A., and Morison, J.: Ensemble 1-year predictions of Arctic sea ice for the spring and summer of 2008, Geophysical Research Letters, 35, 1–5, 2008.